

NASA'S GENESIS AND RAPID INTENSIFICATION PROCESSES (GRIP) FIELD EXPERIMENT

BY SCOTT A. BRAUN, RAMESH KAKAR, EDWARD ZIPSER, GERALD HEYMSFIELD, CERESE ALBERS, SHANNON BROWN, STEPHEN L. DURDEN, STEPHEN GUIMOND, JEFFERY HALVERSON, ANDREW HEYMSFIELD, SYED ISMAIL, BJORN LAMBRIKTSSEN, TIMOTHY MILLER, SIMONE TANELLI, JANEL THOMAS, AND JON ZAWISLAK

As one of three concurrent hurricane field campaigns in 2010, GRIP gathered unprecedented observations—in particular with unmanned Global Hawk flights—to explore the relative importance of environmental and inner-core processes.

In August–September 2010, the National Aeronautics and Space Administration (NASA), the National Oceanic and Atmospheric Administration (NOAA), and the National Science Foundation (NSF) conducted separate but closely coordinated hurricane field campaigns, bringing to bear a combined seven aircraft with both new and mature observing technologies. NASA's Genesis and Rapid Intensification Processes (GRIP) experiment, NOAA's Intensity Forecasting Experiment (IFEX; Rogers et al. 2006, 2013), and NSF's Pre-Depression Investigation of Cloud-Systems in the Tropics (PREDICT) experiment (Montgomery et al. 2012) obtained an unprecedented

set of observations of the formation and intensification of tropical cyclones (TCs), including the storm environment and inner-core regions. NASA, NOAA, and NSF aircraft teamed up to perform coordinated flights for the genesis of Hurricane Karl and Tropical Storm (TS) Matthew and the nonredevelopment of the remnants of Tropical Storm Gaston. NASA and NOAA conducted coordinated flights to thoroughly describe the rapid intensification¹ (RI) of Hurricanes Earl and Karl.

The major goal of GRIP was to better understand the physical processes that control hurricane formation and intensity change, specifically the relative

¹ RI is defined as a 24-h change in wind speed equal to or exceeding 30 kt (15 m s⁻¹) following Kaplan and DeMaria (2003).

AFFILIATIONS: BRAUN AND G. HEYMSFIELD—NASA Goddard Space Flight Center, Greenbelt, Maryland; KAKAR—NASA, Washington, D.C.; ZIPSER AND ZAWISLAK—University of Utah, Salt Lake City, Utah; ALBERS—The Florida State University, Tallahassee, Florida; BROWN, DURDEN, LAMBRIKTSSEN, AND TANELLI—Jet Propulsion Laboratory, California Institute of Technology, Pasadena, California; GUIMOND—Oak Ridge Associated Universities, Oak Ridge, Tennessee, and NASA Goddard Space Flight Center, Greenbelt, Maryland; HALVERSON AND THOMAS—University of Maryland, Baltimore County, Baltimore, Maryland; A. HEYMSFIELD—National Center for Atmospheric Research, Boulder, Colorado; ISMAIL—

NASA Langley Research Center, Hampton, Virginia; MILLER—NASA Marshall Space Flight Center, Huntsville, Alabama
CORRESPONDING AUTHOR: Scott A. Braun, NASA Goddard Space Flight Center, Code 612, Greenbelt, MD 20771
E-mail: scott.a.braun@nasa.gov

The abstract for this article can be found in this issue, following the table of contents.

DOI:10.1175/BAMS-D-11-00232.1

In final form 18 June 2012
©2013 American Meteorological Society

TABLE 1. NASA aircraft information and science flight hours completed.

	Flight altitude range	Endurance (h)	Base of operations	Flight hours completed
DC-8	Up to 40 kft (12.2 km)	8–10	Fort Lauderdale, FL; St. Croix, U.S. Virgin Islands	108.3
GH	55–65 kft (16.8–19.8 km)	Up to 26	Edwards, CA	112.9
WB-57	60–65 kft (18.3–19.8 km)	6	Houston, TX; Tampa, FL	22.9

roles of environmental and inner-core processes. GRIP focused on the following important science questions:

- Do environmental stability and moisture distributions (e.g., the Saharan air layer) play key roles in determining whether disturbances develop or fail to develop into TCs, or is the key factor related to dynamic processes and interaction with environmental vertical wind shear?
- Does the formation of cyclonic vorticity at the surface originate from midlevel cyclonic vorticity that builds downward, or does it originate at low levels and grow upward? What is the role of deep convection in this process?
- If the thermal structure of a vortical disturbance evolves from cold to warm core, then what physical processes are important for generating and maintaining the warm anomaly?
- What environmental (e.g., vertical wind shear, upper-level outflow jets, low- to mid-level moisture, upper-level troughs), oceanic (e.g. warm ocean eddies), and inner-core (e.g., convective bursts, mesovortices) factors govern RI?
- What is the predictability of RI, and what observations are most critical to its prediction?
- Do hot towers and convective bursts play a major role in RI or are they merely indicators of energy conversion processes (e.g., associated with movement over a warm ocean eddy)?

A major focus of GRIP was the application of new technologies to address these important scientific questions, including the first ever use of the unmanned Global Hawk (GH) aircraft for hurricane science operations. Using three different aircraft, NASA brought to the field an array of new instruments as well as older, well-tested technologies. The combined GRIP-IFEX-PREDICT datasets, along with remote sensing data from a variety of satellite platforms

[Geostationary Operational Environmental Satellite (GOES), Tropical Rainfall Measuring Mission (TRMM), *Aqua*, *Terra*, *CloudSat*, and *Cloud-Aerosol Lidar and Infrared Pathfinder Satellite Observations (CALIPSO)*], will contribute to advancing understanding of hurricane formation and intensification. This article describes the NASA contribution to the tri-agency effort to understand better the processes that govern tropical storm formation and intensification. A particular focus is on the value of the new technologies that were brought to the field during GRIP, including the GH platform and some of the new instruments that provided valuable observations during the rapid intensification of Hurricane Karl. Observations from the NASA DC-8 are highlighted in the context of the interaction of Hurricane Earl with the Saharan air layer (SAL). All data from GRIP can be found online (at <http://airbornescience.nsstc.nasa.gov/grip/getdata.html>).

ADVANCED TECHNOLOGIES UTILIZED BY

GRIP. The GRIP campaign extended from 15 August to 25 September and involved three research aircraft (Table 1). The NASA DC-8 has been used in previous NASA hurricane field campaigns including the third Convection and Moisture Experiment (CAMEX-3), the fourth CAMEX (CAMEX-4; Kakar et al. 2006), and the NASA African Monsoon Multidisciplinary Analyses (NAMMA; Zipser et al. 2009).² During GRIP, it was based in Fort Lauderdale, Florida, but it made three deployments to St. Croix in order to reach Hurricane Earl during its RI phase, ex-Gaston during a time of potential redevelopment, and Tropical Storm Matthew in its genesis stage. The DC-8 carried a diverse payload (Table 2), including environmental sensors for aerosols, water vapor, and winds, as well as remote and in situ sensors for inner-core precipitation structure and cloud microphysics. The NASA WB-57 was based out of Houston, Texas, but it occasionally deployed to Tampa Bay, Florida. Its payload consisted of the Hurricane

² Previous NASA hurricane campaigns include CAMEX-3 in 1998 and CAMEX-4 in 2001, the Tropical Cloud Systems and Processes (TCSP) experiment in 2005, and the NAMMA experiment in 2006.

TABLE 2. Instruments by aircraft. LARGE = Langley Aerosol Research Group Experiment. LRC = Langley Research Center. ARC = Ames Research Center. UMBC = University of Maryland, Baltimore County. JPL = Jet Propulsion Laboratory. GSFC = Goddard Space Flight Center. MSFC = Marshall Space Flight Center.			
DC-8	Sensor type	Parameters measured/derived	Principal investigators
LASE	Lidar	Aerosol backscatter and extinction, water vapor mixing ratio, relative humidity, precipitable water	S. Ismail, R. Ferrare/NASA LRC
DAWN	Lidar	Vertical profiles of horizontal wind in clear air	M. Kavaya/NASA LRC
MMS	Rosemont probes	In situ temperature, pressure and wind	P. Bui/NASA ARC
Dropsonde	Aircraft-deployed sondes	Vertical profiles of pressure, temperature, humidity, and winds	J. Halverson/UMBC
Microphysics	Liquid water and ice particle properties	Droplet and ice particle size distributions, particle habit/phase information, presence and amount of supercooled cloud liquid water	A. Heymsfield/NCAR
LARGE	In situ aerosols	Aerosol size distribution, number density, surface area, mass loading, extinction, and single-scattering albedo	B. Anderson, G. Chen/NASA LRC
APR-2	Dual-frequency Doppler radar	3D volumes of radar backscatter, Doppler velocity, and linear depolarization ratio; classification, mean particle size, motion, and total hydrometeor mass	S. Durden, S. Tanelli, E. Im/JPL
Global Hawk			
HIWRAP	Dual-frequency Doppler radar	3D volumes of radar backscatter, Doppler velocity; mean particle size, derived 3D air motions; surface winds in precipitation-free air	G. Heymsfield/NASA GSFC
HAMSr	Microwave sounder	Microwave brightness temperatures in 25 channels, temperature, water vapor, liquid water profiles, and precipitation	B. Lambrigtsen/JPL
LIP	Electric field mills, conductivity probes	Lightning/electric fields	R. Blakeslee/NASA MSFC
WB-57			
HIRAD	Microwave radiometer	Microwave brightness temperatures; surface wind and rain.	T. Miller/NASA MSFC

Imaging Radiometer (HIRAD). The third aircraft was the GH aircraft, which was based at NASA's Dryden Flight Research Center (DFRC) in Southern California and carried the High-Altitude Monolithic Microwave Integrated Circuit (MMIC) Sounding Radiometer (HAMSr), High-Altitude Imaging Wind and Rain Airborne Profiler (HIWRAP), and Lightning Instrument Package (LIP). During the course of GRIP, the GH completed 5 flights, the DC-8 14 flights, and the WB-57 4 flights (Table 3).

The NASA Global Hawk. Perhaps the largest technological advancement during GRIP was the first-time

use of the unmanned high-altitude, long-endurance GH aircraft for hurricane studies. The NASA GH is one of the first series of GHs built by Northrop Grumman Corp. for the U.S. Air Force and was first flown for science measurements by NASA in 2009. The GH length and wingspan are 13.4 m (44 ft) and 35.4 m (116 ft), respectively. It is capable of flight durations of ~30 h, a range of >20,000 km, and flight altitudes of 16.7–19.8 km. The GH's ability to autonomously fly long distances at high altitude for extended periods of time and carry large payloads (up to 1,500 lbs/680 kg) brings a new capability to the hurricane science community for observing remote

locations over the tropical oceans not feasible or practical with other aircraft used for hurricane research and operations (Fig. 1).

Normal autonomous control of the GH is conducted via the aircraft's autopilot system using a preprogrammed mission plan. However, to accommodate the oft-requested changes in flight path by mission scientists, the pilot can alter the flight path at any time and conduct precise manual aircraft navigation with the insertion of custom "way points." At all times, however, the aircraft is under the control of the onboard mission computer that ensures that the aircraft is under controlled flight. The aircraft takes off and climbs very rapidly to 15-km altitude, during which time the instrument investigators check the performance of their instruments. It then gradually climbs to >19 km as it burns off fuel.

Dedicated satellite communication links provide researchers with direct access to their onboard instrument packages during missions. Researchers are able to monitor instrument function from the ground control station and evaluate data in real time. More importantly, the instruments can greatly aid flight operations in terms of targeting storm features and providing real-time data to the science leads.

During GRIP, the GH was deployed from DFRC, the site of NASA's only GH operations center at the time. As a result, all flights to the Atlantic required a ~5-h ferry along the southern border of the United States to the Gulf of Mexico prior to deployment to any particular storm. NASA obtained a mobile GH operations center in 2011 that will allow deployment from anywhere around the globe with a suitable airfield.

TABLE 3. Summary of GRIP flights.

Date/Time	Aircraft	Objectives	Notes
24 Aug	DC8	Sample precipitation along frontal zone, with potential genesis along western tail of front	Underflight of the TRMM Precipitation Radar
28 Aug	GH	Overfly remnants of Hurricane Frank in E. Pacific	First GH flight of GRIP
29 Aug	DC8	Rapid intensification of Earl	Earl intensifies from category 1 to category 2
30 Aug	DC8	Rapid intensification of Earl	Earl intensifies from category 3 to category 4
1 Sep	DC8, WB57	Interaction of Earl with dry air, mature stage structure, and evolution	Earl at max intensity; dry air and arc clouds on western side
2 Sep	DC8, GH	Potential decay stage of Earl	Earl begins decay; first GH flight over a hurricane
6 Sep	DC8	Potential redevelopment of former TS Gaston	Coordinated flight with PREDICT GV
7 Sep	DC8	Potential redevelopment of former TS Gaston	Coordinated flight with PREDICT GV
12 Sep	DC8, GH	Pregensis observations of Karl	Coordinated flights with PREDICT and IFEX
13 Sep	DC8	Pregensis observations of Karl	Coordinated flight with PREDICT GV
14 Sep	DC8, WB57	Pregensis observations of Karl	Coordinated flight with PREDICT GV
16 Sep	DC8, WB57, GH	RI of Karl	GH flies for 14 h over Karl; 20 passes over eye; five aircraft in Karl at once
17 Sep	DC8, WB57	Landfall of Karl	DC8 observes rain structure over Mexico; WB57 observes surface winds in coastal zone
21 Sep	DC8	Pregensis of Matthew	Coordinated flight with PREDICT GV
22 Sep	DC8	Pregensis of Matthew	Coordinated flight with PREDICT GV
23 Sep	GH	TS Matthew	GH observes highly asymmetric structure of Matthew

New or improved instruments. GRIP introduced several new instruments to the hurricane research endeavor. The HIWRAP instrument (Li et al. 2011; see Table 2) is a dual-frequency [Ka band (35 GHz) and Ku band (14 GHz)], dual-beam (30° and 40° incidence angles), conically scanning Doppler radar designed for operation at high altitudes. The Ku frequency matches that on the TRMM satellite, and both frequencies will be used on the Global Precipitation Measurement (GPM) mission to be launched in 2014. HIWRAP provides information on precipitation and three-dimensional winds within raining areas and ocean surface wind vectors in rain-free or light-precipitation areas via scatterometry techniques. HIWRAP flew with HAMSR (a microwave sounder described below) and the LIP on the GH.

The HIRAD sensor (Amarin et al. 2012) on the WB-57 is a single polarization, passive C-band radiometer that measures wind speeds and rainfall at the ocean surface. The measurement is similar to the Stepped-Frequency Microwave Radiometer (SFMR)

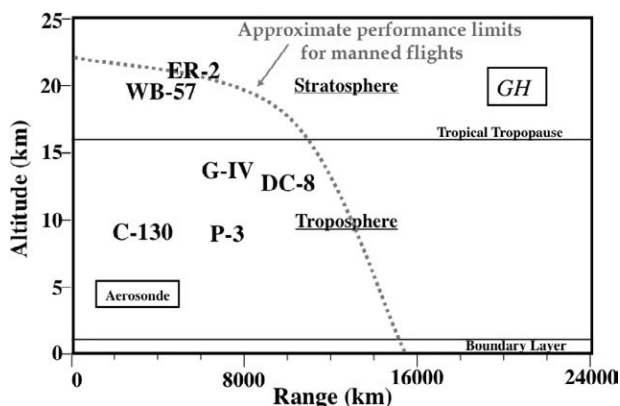


FIG. 1. Approximate range and maximum flight altitude for aircraft used for hurricane science or reconnaissance flights, including the NASA ER-2, WB-57, DC-8, and GH; NOAA G-IV and P-3; Air Force C-130; and Aerosonde. Bold lettering indicates payload capacity greater than 2,000 lbs (907 kg), and italics for capacity between 1,000 and 2,000 lbs (454–907 kg). Dotted line indicates an estimate of the altitude and range limits for manned flights. Unmanned aircraft are enclosed in boxes.

NEW HURRICANE IMAGING TECHNOLOGY

The HIRAD instrument, which flew on the NASA WB-57 aircraft, will ultimately have SFMR-type capability but with cross-track scanning that will greatly enhance coverage of wind speed estimates in the hurricane inner core. Calibration of the radiances is ongoing, and wind speed retrievals are not currently available. However, brightness temperature (T_b) information can provide information on storm structure. During the intensification of Karl, the WB-57 crisscrossed the eye multiple times on 16 September, providing an excellent example of HIRAD data in an intense storm (Fig. SBI). Preliminary data consist of “excess” brightness temperatures that are indicative of rain and wind fields. The excess brightness temperatures clearly indicate the location of the eyewall as well as an inner rainband to the south of the eye, an outer rainband to the southwest, and more broken precipitation to the north of the eyewall. Upon completion of the final calibration of each microwave

channel, full retrievals of the wind speed and precipitation fields will be available.

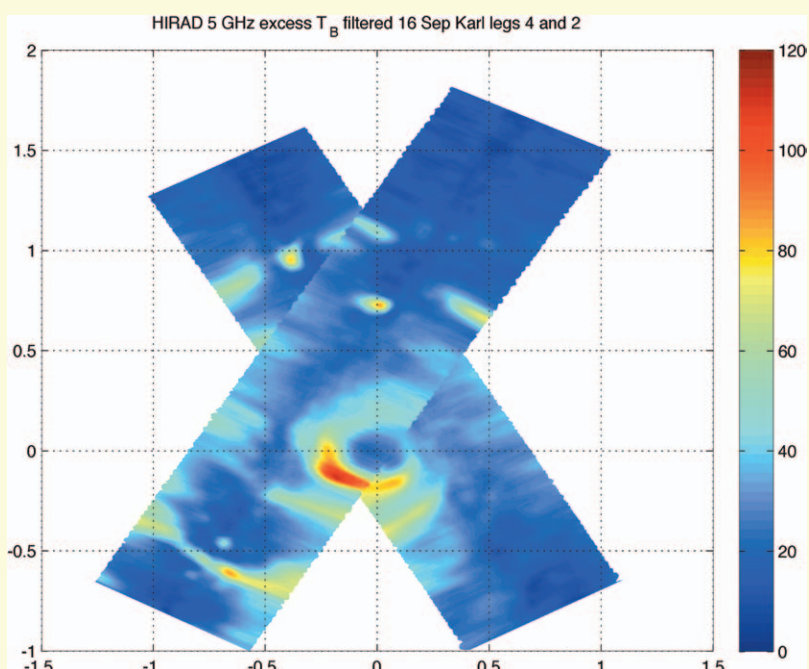


FIG. SBI. HIRAD-observed 5-GHz excess T_b over Karl on 16 Sep. Swath on top was obtained first, 1901:14–1926:39 UTC. Swath underneath was from 1943:50 to 2006:20 UTC. Coordinates are latitude and longitude relative to storm centers as determined by HIRAD, which were 19.74°N, 93.38°W at 1916:49 and 19.76°N, 93.46°W at 1952:37 UTC. Excess T_b is the observed T_b minus the modeled background T_b for a calm ocean as a function of off-nadir angle. High values of excess T_b at this frequency indicate strong surface winds and/or rain.

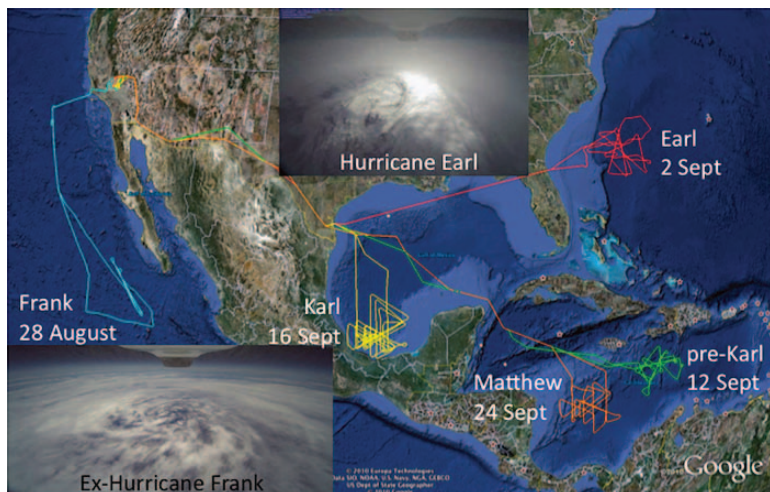


FIG. 2. GH flights summary showing aircraft flight tracks during the five GH missions. Also included are views of (bottom left) Frank and (top) Earl from the GH high-definition camera.

utilized on the NOAA P3 aircraft but with cross-track scanning to provide a swath of wind speed information rather than just a line of wind data.

The Doppler Aerosol Wind (DAWN) lidar (Koch et al. 2010) uses a 2- μm laser, whose light is backscattered by natural aerosols and cloud particles that move with the wind. The measurements are converted to line-of-sight winds at five different azimuth angles, allowing retrieval of the horizontal and vertical wind components. DAWN flew on the DC-8 aircraft and complemented other environmental sensors (see Table 2), such as the Lidar Atmospheric Sensing Experiment (LASE; Browell et al. 1997) and the dropsonde system.

An older but improved instrument for GRIP, HAMSR is a cross-track scanning microwave sounder (Brown et al. 2011) that has been used in previous NASA experiments, including CAMEX-4, TCSP, and NAMMA. HAMSR was extensively upgraded in 2008 with improved state-of-the-art receiver technology and a data system that provides real-time access to the observations during flight. The instrument improvements have eliminated a dry bias above 4-km altitude noted by Brown et al. (2007). The real-time capability provides situational awareness that was exploited during GRIP to attain 20 consecutive passes over the eye of Hurricane Karl during a 14-h period, nearly all of them passing very near the center of the storm. HAMSR operates with 25 channels in three spectral bands near the 50- and 118-GHz oxygen lines and near the 183-GHz water vapor line, with 8, 10, and 7 channels, respectively.

Another older but improved instrument used during GRIP was the second-generation Airborne Precipitation Radar (APR-2; see Sadowy et al. 2003).

The APR-2 had an improved radome designed to minimize signal loss at both frequencies (i.e., Ku band and Ka band) and to improve its Ka-band sensitivity (confirmed improvement of ~ 5 dB) and signal purity at Ka band in the Doppler and cross-polarization measurements. APR-2 also implemented for the first time a real-time visualization software package that enabled the science team on the DC-8 to assess within minutes the structure of precipitating systems and the locations of the storm center.

GRIP ACCOMPLISHMENTS.

Demonstration of the GH for hurricane research. The GH was originally

designed for military surveillance in clear-sky conditions and was not intended for weather reconnaissance. Over-storm turbulence was a particular concern heading into GRIP operations given previous encounters with strong turbulence during an ER-2 flight over Hurricane Emily (2005) during NASA's TCSP experiment (Halverson et al. 2007). The concept of operations prior to the first flight was that the pilots, before attempting to cross over a hurricane, would "test the waters" for turbulence by gradually flying inward from the edges of the cloud system. If no turbulence was encountered, then they would continue gradually inward.

As an initial test, the first GH flight during GRIP was over the relatively benign remnants of Hurricane Frank in the eastern Pacific on 28 August. With relatively low cloud tops and little deep convection, turbulence concerns were negligible. The GH conducted five southeast-to-northwest flight legs of ~ 380 -km length over the center of Frank, getting a view from high altitudes of the decaying storm (Fig. 2).

The first hurricane flight for the GH was on 2 September as category 4 Hurricane Earl was at peak intensity but beginning to weaken as it moved northward off the southeastern U.S. coastline. Because a 1 September flight of the WB-57 encountered no turbulence at flight altitude (the same altitude as the GH), the GH pilots sent the aircraft directly over the storm (Fig. 2), allowing coordinated flights between the GH, DC-8, and NOAA P-3. Three other flights of the GH occurred during GRIP, with the GH overflying convective systems during the genesis phase of Karl, a historic 20 overpasses of the eye during a flight over rapidly intensifying Karl, and a final

flight over Tropical Storm Matthew to close out the GRIP experiment.

The overflight of Hurricane Karl during its rapid intensification on 16–17 September is used here to highlight some of the key advantages of using the high-altitude, long-endurance GH aircraft. Karl made landfall on 14 September on the Yucatan Peninsula as a strong tropical storm with estimated winds of 27 m s^{-1} , emerging from the Yucatan 2 days later significantly weaker (17 m s^{-1}). Despite its passage over land, Karl was still well organized with TRMM

85-GHz polarization-corrected temperatures (PCTs), suggesting an eyewall structure and possible eye (Fig. 3a). As Karl moved over the southern Bay of Campeche, it rapidly intensified from ~ 23 to 56 m s^{-1} in 30 h, making landfall on the coast of Mexico on 17 September as a category 3 hurricane. During the rapid intensification phase, NASA, NOAA, and U.S. Air Force aircraft sampled the storm in record numbers, with up to five aircraft in the storm at one time. Aircraft tracks (Fig. 3b) demonstrate the extraordinary sampling of the storm on this day.

ECS PARTICIPATION AND SUPPORT DURING GRIP

Early career scientists (ECSs) filled many science team roles and made significant contributions that were integral to the success of GRIP, just as they were to PREDICT (Evans et al. 2012). These roles included forecasting, mission science, data management, and instrument operations. As has been the experience in previous field campaigns, ECS participation not only greatly supports the ultimate success of the field program, but it also benefits the ECSs themselves, as they gain valuable experiences that can be applied toward developing and achieving their research and career goals.

One of the most vital ECS contributions to GRIP was forecasting support. The forecast team was tasked with communicating forecast briefings; consulting with mission scientists on aircraft schedules and mission flight plans; communicating disturbance center positions and potentially hazardous conditions to mission and platform scientists during aircraft operations; and downloading, quality controlling, and transmitting/archiving DC-8 dropsonde data in real time. Forecast briefings for daily GRIP science team meetings and tri-agency briefings (in rotation with PREDICT and IFEX forecasters) were produced and led by GRIP student forecasters. In preparing briefings, forecasters had to be aware of multiple disturbances, often initiating important

discussions with mission scientists to decide which targets to investigate. Some ECSs even arrived with their own supplemental model and analysis products, while all brought valuable knowledge to the forecast team. This unique collaboration and free exchange of ideas between the ECSs, under the guidance of mission scientists, is one of the most rewarding aspects of field experiment participation.

Many ECSs also contributed to data collection as instrument scientists, engineers, and operators. In fact, the dropsonde system on the DC-8 was largely operated by ECSs (Fig. SB2). Even for those without instrument responsibilities, the availability of seats on the DC-8 provided a unique opportunity for ECSs to observe the impressive cooperation required between the flight crew, instrument operators, and platform scientists in order to complete the mission objectives, while understanding each role's tasks and challenges. Many theses, dissertations, and publications authored by ECSs will be greatly enhanced by the knowledge gained through their participation in GRIP. Without a doubt, the various roles assumed by ECSs, as well as the numerous interactions with their peers and mentors, will be important and unparalleled building blocks in their career development.

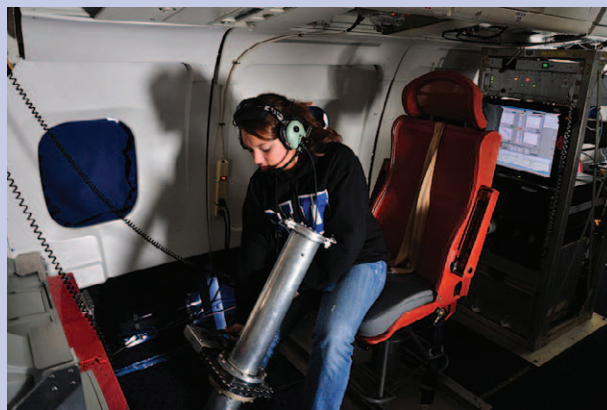


FIG. SB2. (left) Graduate students (from left to right) Janel Thomas, Cerese Albers, Jon Zawislak, Andrew Martin, Leon Nguyen, and Diana Thomas on board the NASA DC-8. (right) Janel Thomas prepares a sonde for release from the DC-8.

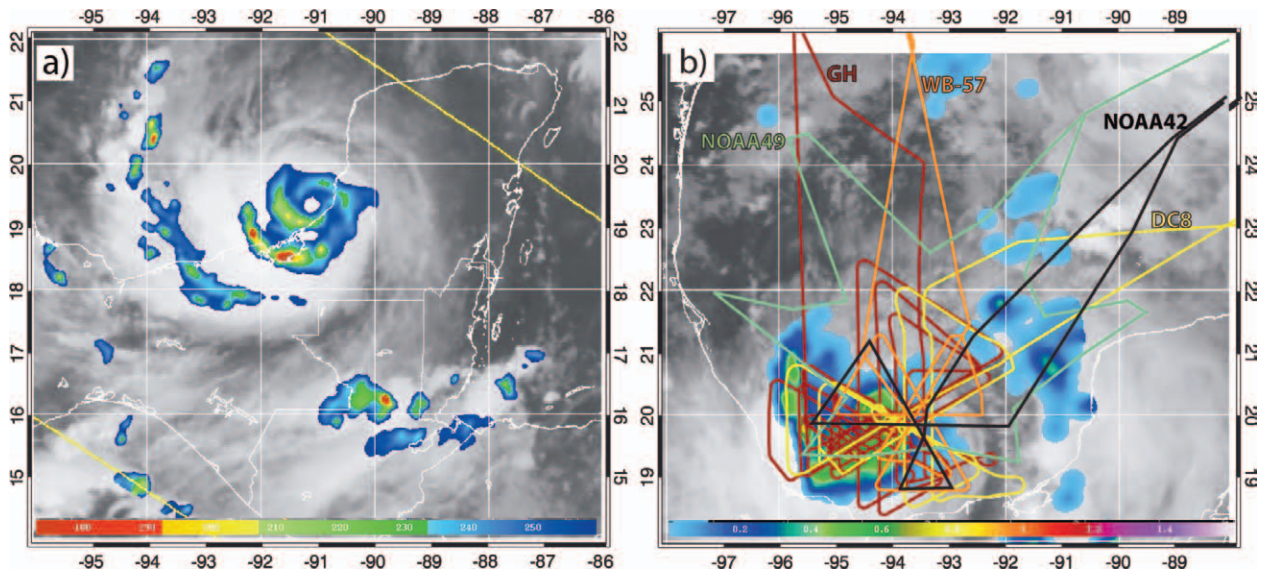


FIG. 3. (a) GOES infrared image at 0615 UTC and TRMM Microwave Imager 85-GHz PCT for 0603 UTC 16 Sep. (b) GOES infrared image at 0110 UTC and Special Sensor Microwave Imager (SSM/I) rain rate for 0113 UTC 17 Sep. Flight tracks for NASA and NOAA aircraft indicate the extensive airborne sampling of Karl's RI phase (dark red, GH; orange, WB-57; yellow, DC-8; black, NOAA P-3; light green, NOAA G-IV). GOES images are from the Naval Research Laboratory (NRL)'s tropical cyclone (TC) web page (www.nrlmry.navy.mil/TC.html).

The GH flight was unprecedented for its 20 crossings of the eye over the approximately 14 h that it was on station over Karl. The HIWRAP radar offers the potential to map the wind and precipitation fields within the hurricane inner core over the course of such long flights. While the wind fields from this case are still very preliminary, Fig. 4 provides an example of the derived horizontal wind speed field at 3-km altitude in Hurricane Karl as it was undergoing rapid intensification. During this flight, only the inner (30° incidence angle) beam was operational, so the swath of wind speed information is about one-third narrower than would normally be the case. In order to show data over a 12-h window during the flight, only the north-to-south passes are shown. The HIWRAP data show that the strongest winds were generally on the northeastern to northern side of the storm with magnitudes of about 40–45 m s⁻¹ near 1900 UTC 16 September and increasing quickly to near or above 60 m s⁻¹ after 0000 UTC 17 September.

HAMS observations provide detailed measurements of the evolution of the warm core during rapid intensification. Temperature and water vapor profiles are retrieved from HAMS using an optimal estimation-based retrieval algorithm (Brown et al. 2007). A DC-8 dropsonde profile and two HAMS

profiles (Fig. 5) from three different crossings of the eye of Hurricane Karl on 16–17 September show the evolution of the warm core during Karl's rapid intensification. One profile represents the DC-8 dropsonde at 2029 UTC 16 September and the two other profiles represent HAMS retrievals at 0009 and 0804 UTC 17 September. Prior to 2100 UTC, the eye was partially filled and significant scattering caused by ice degraded retrievals at earlier times. The HAMS retrievals in the lowest few kilometers in the eye (below 750 mb) should be treated with caution, as they are susceptible to uncertainties in emissivity resulting from sea surface roughness and foaming (Uhlhorn and Black 2003) and potentially from the presence of low-level clouds in the eye. These effects tend to produce a warm and moist bias in the HAMS retrievals below 750 mb, which may explain the large differences from the dropsonde profile at lower levels. Correction of these biases is an area of ongoing work. The effect of these error sources on the retrievals quickly diminishes above 750 mb.³

At 2030 UTC 16 September, the DC-8 sounding showed a deep moist layer in the eye extending up to ~750 hPa topped by a strong inversion. Dewpoint depressions in the 700–600-hPa layer were ~5.5 K (corresponding to a relative humidity of ~70%), while values at upper levels were ~1–1.5 K (80%–90%). The

³ Based on comparisons with 50 dropsondes from the GH in a wide array of midlatitude environments during 2011 test flights, HAMS was found to have a root-mean-square error of 2 K for temperature and 16.5% for relative humidity (S. Brown 2012, personal communication).

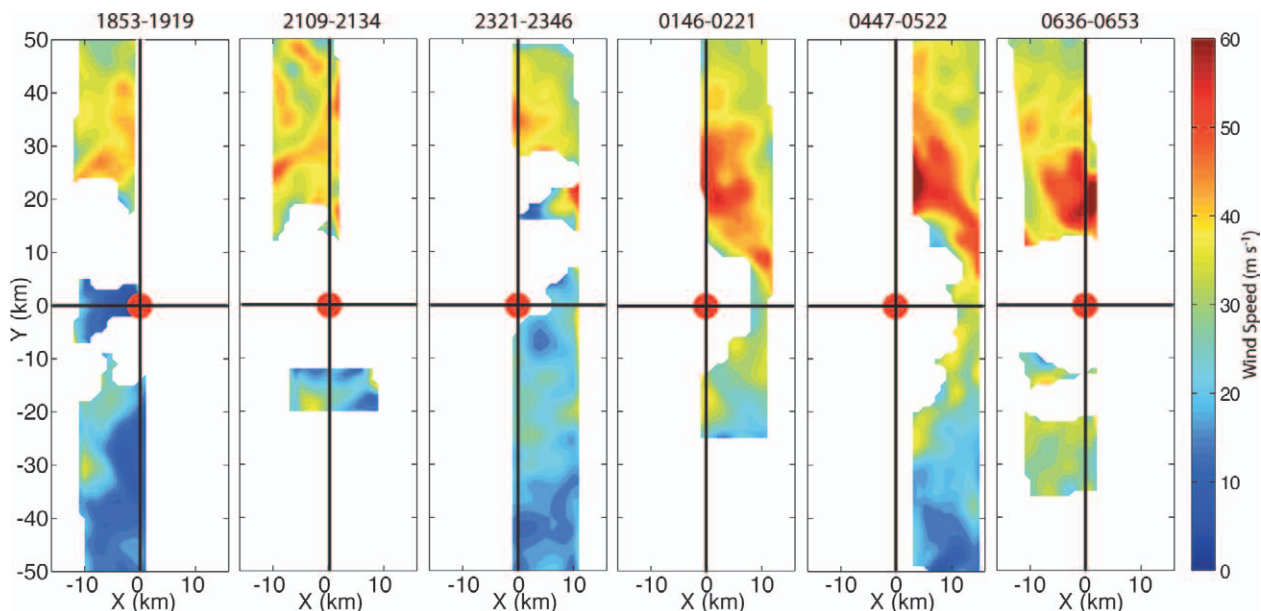


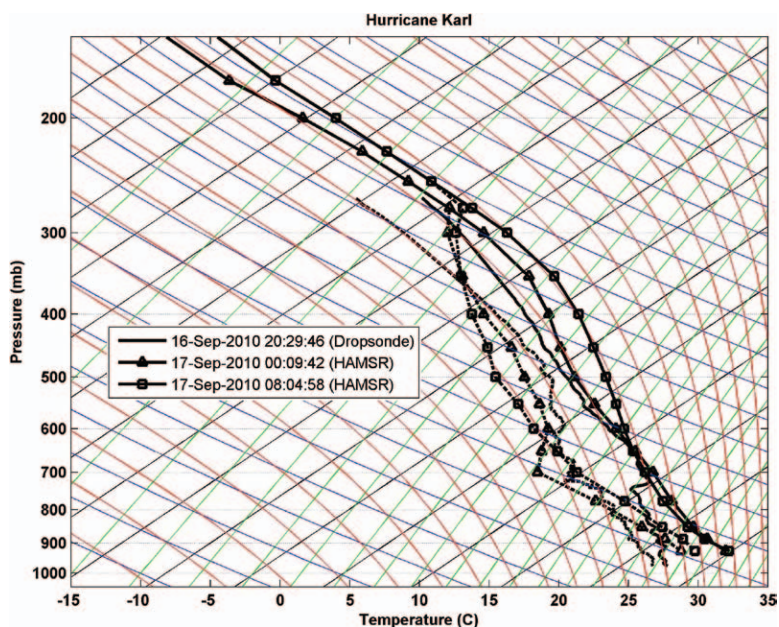
FIG. 4. Preliminary analysis of HIWRAP-derived horizontal wind speeds at 3 km for several of the north-south passes through Karl. Time span (in UTC on 16–17 Sep) for each leg is indicated at the top of each panel. The red circle indicates the approximate storm center position, and solid lines oriented north-south and west-east are drawn through the center. Over the ~12-h period, wind speeds increased from ~42 m s⁻¹ to slightly more than 60 m s⁻¹.

two HAMSRS profiles corresponding to 0000 and 0800 UTC 17 September show significant warming above 700 hPa during the 8-h interval between the soundings, with the peak increase occurring in the 500–400-hPa layer. Strong warming extending up to near 300 hPa is apparent when the 0800 UTC HAMSRS profile is compared to the DC-8 dropsonde profile. The warming is accompanied by a marked decline in dewpoint temperatures in the 600–400-hPa layer.

Figure 6a shows the best-track minimum pressure from the National Hurricane Center (NHC) Tropical Cyclone Report (available online at www.nhc.noaa.gov/2010atlan.shtml) for the period of the GH flight over

Karl along with time series of the HAMSRS-derived temperature anomaly⁴ at 7- and 12-km altitude. Karl was undergoing steady deepening at an average rate of ~8 hPa per 6 h during the period. HAMSRS temperature anomalies at 7 km increased steadily by 3 K over the period, while at 12 km the temperature anomaly was relatively flat until 0300 UTC but

FIG. 5. Skew *T* diagram showing profiles from the inner core of Hurricane Karl during RI. The 2000 UTC 16 Sep profile is from a DC-8 dropsonde and the 0000 and 0800 UTC 17 Sep profiles are from HAMSRS. Solid lines are temperature, and dashed lines are dewpoint temperature. HAMSRS profiles below 750 hPa should be viewed with caution because of warm and moist biases described in the text.



⁴ The anomaly was determined by subtracting a constant-in-time reference profile determined by averaging HAMSRS data during the inbound flight leg at a distance 225–250 km from the storm center.

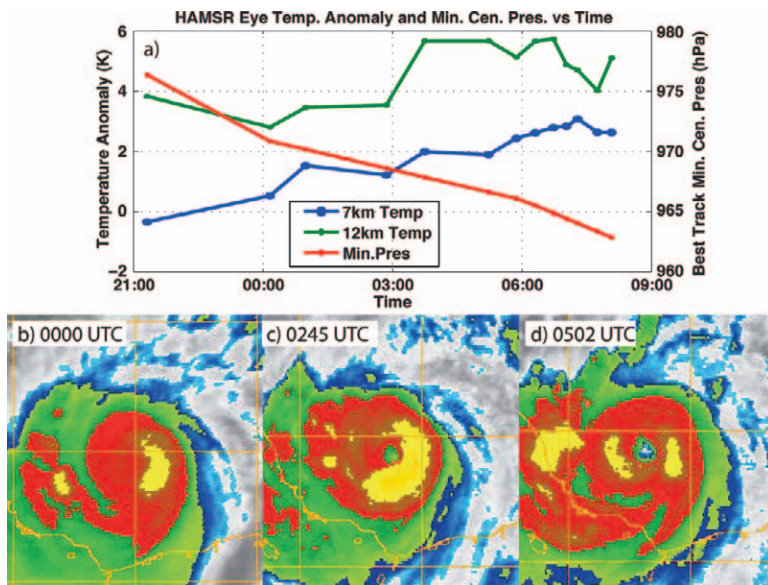


FIG. 6. (a) Time series of best-track minimum sea level pressure (available from www.nhc.noaa.gov/2010atlan.shtml) and temperature anomalies (see footnote 4 on the previous page) at 7- and 12-km altitude from HAMS on 16–17 Sep. (b)–(d) GOES infrared images from the NRL TC web page on 17 Sep at the indicated times showing the formation of the clear eye in the upper-level clouds.

then increased markedly. This period of upper-level warming corresponded to the formation of a clear eye in GOES satellite imagery (Figs. 6b–d), suggesting that the high-level warming was tied to enhanced upper-level subsidence that led to the clearing of the clouds previously covering the eye.

The GH flight over Karl demonstrates the unique capability and potential science gain associated with a high-altitude, long-endurance airborne platform. The ability to sample a storm for 14 h or more and observe changes in wind and thermodynamic structure over the depth of the troposphere makes possible the measurement of processes such as upper-level eye warming and its connection to an evolving inner-core wind field. Of the five GH flights during GRIP, the Karl RI flight was by far the most scientifically valuable. The last GH flight over Tropical Storm Matthew will also be of high value for examining the response of a newly formed storm to large environmental wind shear (discussed briefly below).

DC-8 observations of the RI of Hurricane Earl in the presence of Saharan air. Hurricane Earl was one of three major hurricanes in 2010 that underwent RI in the presence of prominent SAL outbreaks (along with Igor and Julia), but it was the only one sampled during GRIP. The impact of the SAL on the development and intensification of TCs has garnered significant attention in recent years. Early studies

(e.g., Karyampudi and Carlson 1988; Karyampudi and Pierce 2002) suggested a potential positive influence of the SAL on tropical cyclogenesis via influences on African easterly wave (AEW) growth and support of convection at its leading and southern borders (where low-level cyclonic shear is largest). In contrast, Dunion and Velden (2004) focused on mechanisms that generally inhibit TC genesis and intensification, including suppression of convection by an enhanced low-level temperature inversion, increased vertical wind shear associated with the African easterly jet, and intrusions of dry SAL air into TCs. Braun (2010b) found the SAL to be an integral part of the hurricane environment at the time of tropical storm formation for both strengthening storms and weakening storms (in the 2–4 days after storm formation), suggesting that the SAL

is not a major determining factor in the intensity changes after storm formation. The disagreement between the results of Karyampudi and collaborators, Braun (2010b), and Dunion and Velden (2004) raises major questions regarding the role of the SAL in the genesis and intensity change of individual storms. Here, we highlight some of the observations collected on the NASA DC-8 that may yield insights into the role of the SAL in the case of Hurricane Earl.

Hurricane Earl formed from a strong wave that moved off of the African coast on 23 August in association with a prominent SAL air mass. By midday on 25 August, the wave had become Tropical Storm Earl at a time when the storm had extensive dust on its western and northern sides. Over the next 4 days, Earl gradually became stronger and better organized as it tracked westward with the SAL, becoming a hurricane at 1200 UTC 29 August. The onset of rapid intensification began at approximately 0000 UTC 29 August and ended around 1800 UTC 30 August, with peak winds increasing over that period from 28 to 59 m s⁻¹. Saharan dust was observed with the LASE lidar on board the DC-8 in the environment of Earl throughout its life cycle.

That Earl underwent RI while SAL air was present in the near environment can be understood in a context similar to the hypothesis of Dunkerton et al. (2009). They developed the concept of a protective wave “pouch” that protects an incipient vortex from

deleterious influences of its environment. In a reference frame moving with the disturbance, a set of approximately closed material contours exists within which air tends to be repeatedly moistened by convection and protected to some degree from intrusions of dry air and deformation by horizontal or vertical shear. This pouch theory formed the scientific basis for the PREDICT field campaign (Montgomery et al. 2012). In the case of a more mature storm, such as Earl, such closed streamlines likely still act to protect the stronger vortex in the inner-core region. Storm-relative streamlines in the 850–700-hPa layer from the National Centers for Environmental Prediction (NCEP) Global Forecast System (GFS) final analyses at 1800 UTC 29 August (Fig. 7a) and 30 August (Fig. 7b), combined with Advanced Microwave Scanning Radiometer for Earth Observing System (AMSR-E) total precipitable water data, suggest that dry SAL air, at best, had a slow route inward toward the inner-core region of Earl.

Flights of the NASA DC-8, along with the NOAA P-3 and Gulfstream IV (G-IV) as part of IFEX, were conducted on these days during the period of RI. Relative humidity data at 700 hPa on 29 August from the G-IV and DC-8 (Fig. 7a) agree with the AMSR-E data in showing a very moist inner-core region and dry air confined to much larger radii (>200–300 km). On 30 August (Fig. 7b), LASE data along the inbound flight toward Earl clearly indicated the presence of Saharan dust right up to an outer rainband on the northwestern side of the storm. The close-up view of the LASE data in Fig. 7c shows that the dust layer depth is ~2.5 km at the beginning of the cross section and becomes shallower until 1751 UTC (hour 17.85). At that point, it increases sharply in depth before becoming shallower again. This discontinuity in the dust layer is an interesting feature. The deeper dust layer just after 1751 UTC is embedded near the western edge of a more moist air mass closer to the storm,

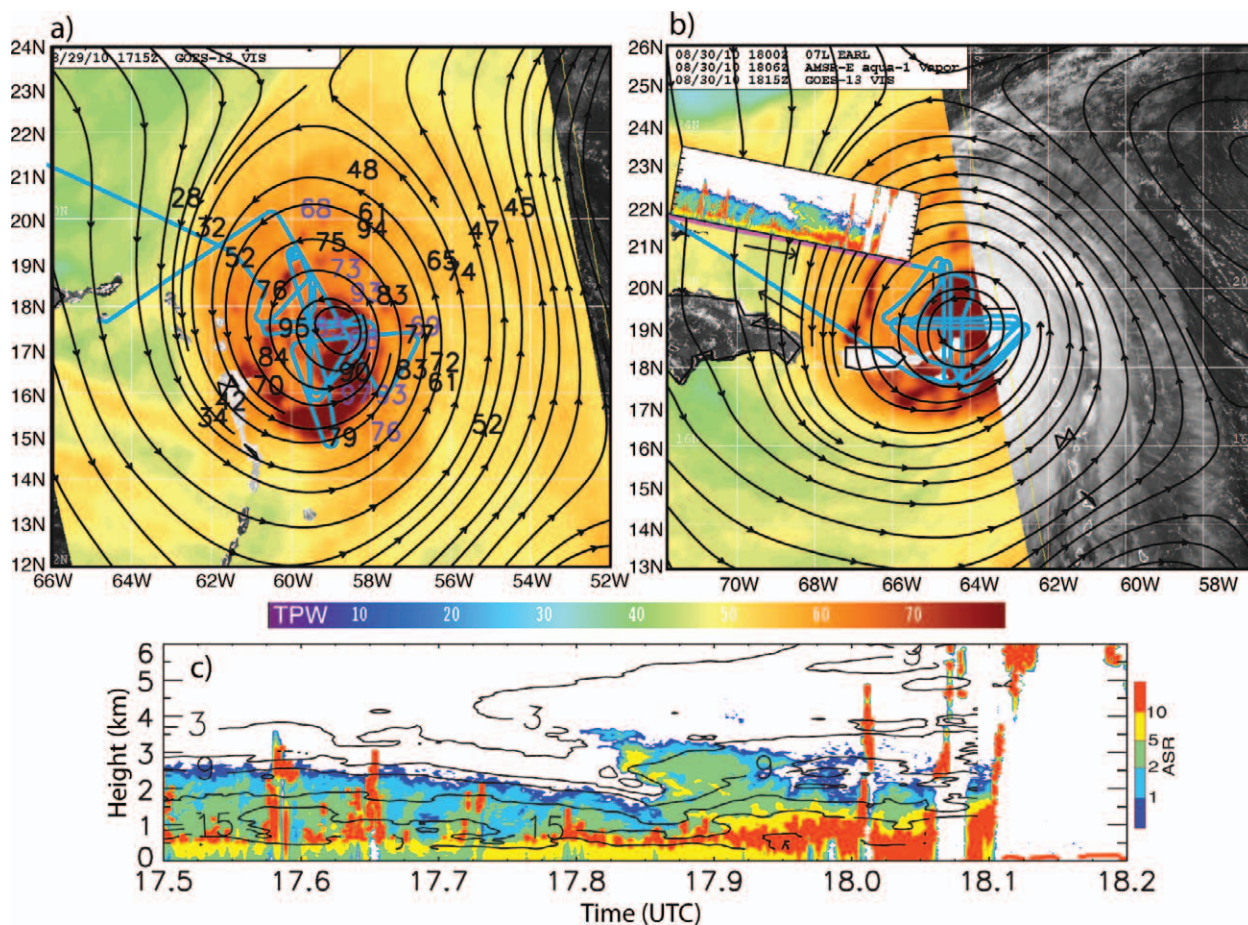


FIG. 7. NCEP GFS 1800 UTC storm-relative streamlines for the 850–700-hPa layer and AMSR-E total precipitable water at (a) 1723 UTC 29 Aug and (b) 1806 UTC 30 Aug. DC-8 flight tracks for each day are shown. In (a), 700-hPa relative humidity values from the DC-8 (purple) and NOAA G-IV (black) dropsondes, with positions adjusted for storm motion, are superimposed. (c) LASE aerosol scattering ratio and vapor mixing ratio (3 g kg⁻¹ intervals) on the inbound flight leg on the western side of Earl [purple section of flight track and inset in (b)] indicate the presence of Saharan dust. Satellite images are from the NRL TC web page.

with vapor mixing ratios above 2 km about $2\text{--}4\text{ g kg}^{-1}$ higher than to the west (prior to 1751 UTC). The driest air in the 2–4-km layer [between 1742 (hour 17.7) and 1751 UTC] is dust free, suggesting a non-SAL source of dry air likely associated with subsidence, similar to that described by Braun (2010a).

A particular focus for the 30 August DC-8 flight was a set of repeated, nonrotating Fig. 4 patterns (Fig. 7b) designed for calculating time rates of change of measured quantities during RI. The APR-2 Doppler radar data highlight some of the changes in storm structure occurring during these repeated passes

through the storm. Near this time, NCEP GFS analyses indicated deep-layer mean vertical wind shear from the north-northwest of $\sim 6\text{ m s}^{-1}$, with most of that shear occurring in the layer above 500 hPa (not shown). Figure 8 shows cross sections of radar reflectivity and vertical motion during the first and third north-to-south passes across the eye. During the first pass (Figs. 8a,b), a small southward tilt of the eye/eyewall was apparent, with intense reflectivities and strong upward motions on the downshear (southern) side and descending motions on the upshear (northern) side, consistent with previous observational and modeling

studies (e.g., Frank and Ritchie 1999, 2001; Reasor et al. 2000; Corbosiero and Molinari 2002; Braun and Wu 2007). Note that here the tilt is being determined from the reflectivity contours, whereas the previous studies have generally used the vorticity or wind field to define storm tilt. By the time of the third pass (Figs. 8c,d), the tilt had increased. While ascending motion dominated the downshear side of the storm, convection was fairly weak, as indicated by the weak reflectivities and vertical motions. On the upshear side, descending motions were still prevalent at middle to upper levels, although strong updrafts were present at lower- and uppermost levels. Very little tilt of the eye/eyewall was apparent in the east-to-west passes (not shown). Thus, the apparent tilt, based on the reflectivity data, was slightly downshear right, while many studies have shown that storm tilts are more often downshear left or left of the shear (Reasor et al. 2004; Braun et al. 2006; Reasor and Eastin 2012). Whether this downshear-right tilt is real, is related to errors in the GFS-analyzed shear, or arises from the use of reflectivity rather than vorticity to estimate tilt is a topic for further investigation.

Given the proximity of the dusty air near Earl on these days, was there any evidence to suggest that the aerosols were present in cloud updrafts and affecting microphysical properties? Conceptually, aerosols might affect cloud microphysical properties by acting as cloud

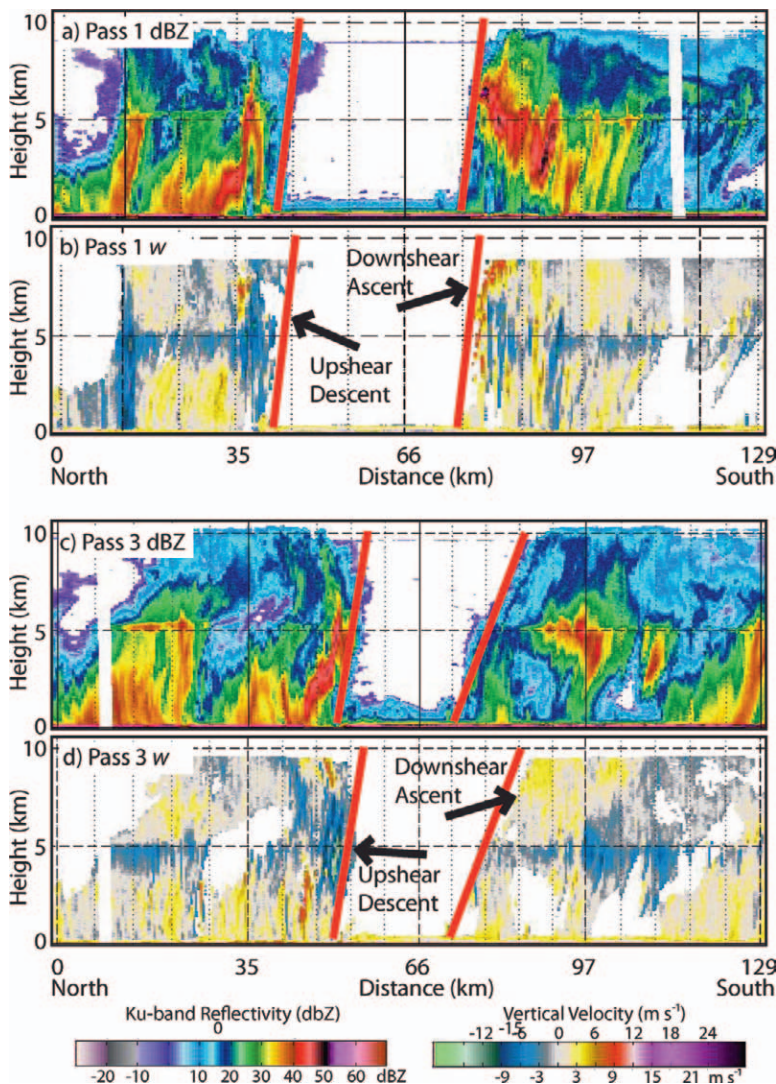


FIG. 8. Reflectivity and vertical motion in the (a),(b) first and (c),(d) third north-to-south passes on 30 Aug showing the southward eyewall tilt and related vertical structures. Fields shown are (a),(c) reflectivity and (b),(d) vertical motions. Red lines indicate the approximate inner edges of the eyewall. The apparent change in eye diameter between the two passes is likely because the first pass was directly through the center, while the third pass was $\sim 5\text{--}8\text{ km}$ east of the center.

condensation nuclei and spreading cloud liquid water over a much greater number of smaller drops than in aerosol-free air (Gunn and Phillips 1957; Rosenfeld 1999). Such a process can be detected by the Cloud Droplet Probe (CDP, sizing from about 2 to 50 μm ; see Lance et al. 2010) on the DC-8 when high concentrations of cloud droplets in the 3–10- μm -diameter range are observed.

CDP data from the six storm crossings on the 30 August flight did not indicate a clear impact on the cloud microphysics. The first of the six flight legs detected high concentrations of small drops, the second detected only a slight enhancement, while the remaining four legs saw no enhancement of small drops. The reason for the differences appears to be that the first two crossings

of the storm were at temperatures (outside of the eye) warmer than -40°C , while the others were colder than -40°C (where liquid water quickly freezes). Data from the CDP instrument for the first flight leg are shown in Fig. 9 along with corresponding data from the APR-2 radar and the Meteorological Measurement System (MMS) in situ measurements (Chan et al. 1998). The radar reflectivity during this pass is identical to that in Fig. 8a. Both the northern and southern sides of the eyewall contained strong updrafts at flight level (~ 240 hPa, 10.7 km) of 8–11 m s^{-1} and liquid water contents of about 0.1 g m^{-3} . However, high concentrations of small drops were present only in the southern eyewall. An important question for future study is how the aerosol survived removal by precipitation to reach the upper troposphere in an eyewall.

The DC-8 conducted additional flights on 1 September (with the WB-57, Fig. 10a) and 2 September (with the GH, Fig. 10b). Prior to these flights, on 31 August, Earl had undergone an eyewall replacement cycle that led to a small weakening of

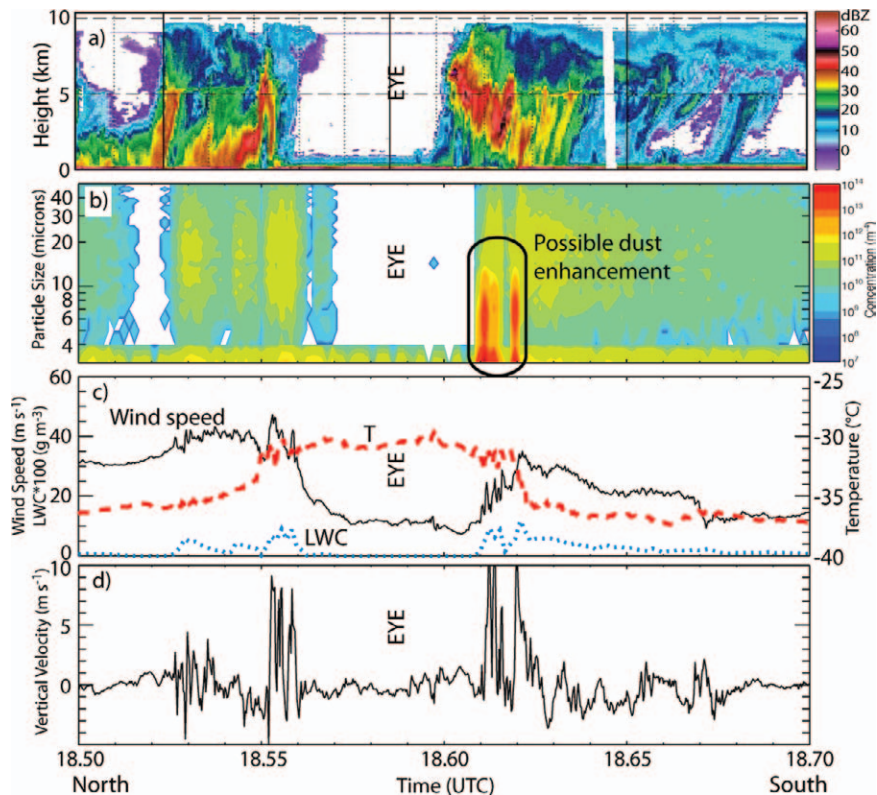


FIG. 9. (a) APR-2 radar reflectivity; (b) cloud droplet concentrations in the range of 3–50 μm from the CDP; (c) in situ wind speed, temperature, and liquid water content; and (d) vertical velocity for the first north-to-south pass on 30 Aug. Eye of the storm is clearly indicated by the warm temperatures between the eyewall wind speed maxima. Flight-level for in situ data in (b)–(d) was ~ 10.7 km.

the storm (Fig. 10f). During the 1 September flights, Earl reintensified and reached its maximum overall intensity early on 2 September before beginning a final weakening stage during the 2 September flights as the storm came under the influence of increasing southwesterly vertical wind shear. LASE aerosol profiles during these flights showed abundant dust on the western side of the storm extending up to 3–4-km altitude (Figs. 10c–e). Although cloud cover generally prevented LASE aerosol observations on the eastern side of the storm, the portion of the flight legs farthest from Earl to the southeast on 1 September indicated aerosols extending up to 2-km altitude (not shown). Therefore, Earl underwent RI and maintained major hurricane intensity while surrounded by Saharan dust over most of its life cycle.

Similar to the first leg of the 30 August flight, CDP observations on 1–2 September clearly showed aerosol-enhanced concentrations of small, liquid drops [as corroborated by the Rosemount icing detector (RICE) probe]. Large numbers of small drops (3–10 μm) were observed by CDP during three of four crossings of

the storm on 1 September and four of five crossings on 2 September. An example is shown in Fig. 11 for a west-to-east transect across the storm on 2 September. Consistent with the satellite image in Fig. 10b, the APR-2 radar observed an inner-eyewall feature and outer rainband feature. The inner eyewall was characterized by very weak radar reflectivities located just inside the peak flight-level wind speeds, with the eastern side having echoes only above about 6 km. This

upper-level echo associated with the eastern eyewall is where CDP observed very high concentrations of drops of about 5–6- μm diameter. It was coincident with high supercooled liquid water contents and vertical motions of 5 m s^{-1} , and produced reflectivities of nearly 30 dBZ near 8 km but little reflectivity below. This structure might suggest a delay in precipitation formation associated with the presence of high concentrations of aerosols. In the western eyewall and in the outer

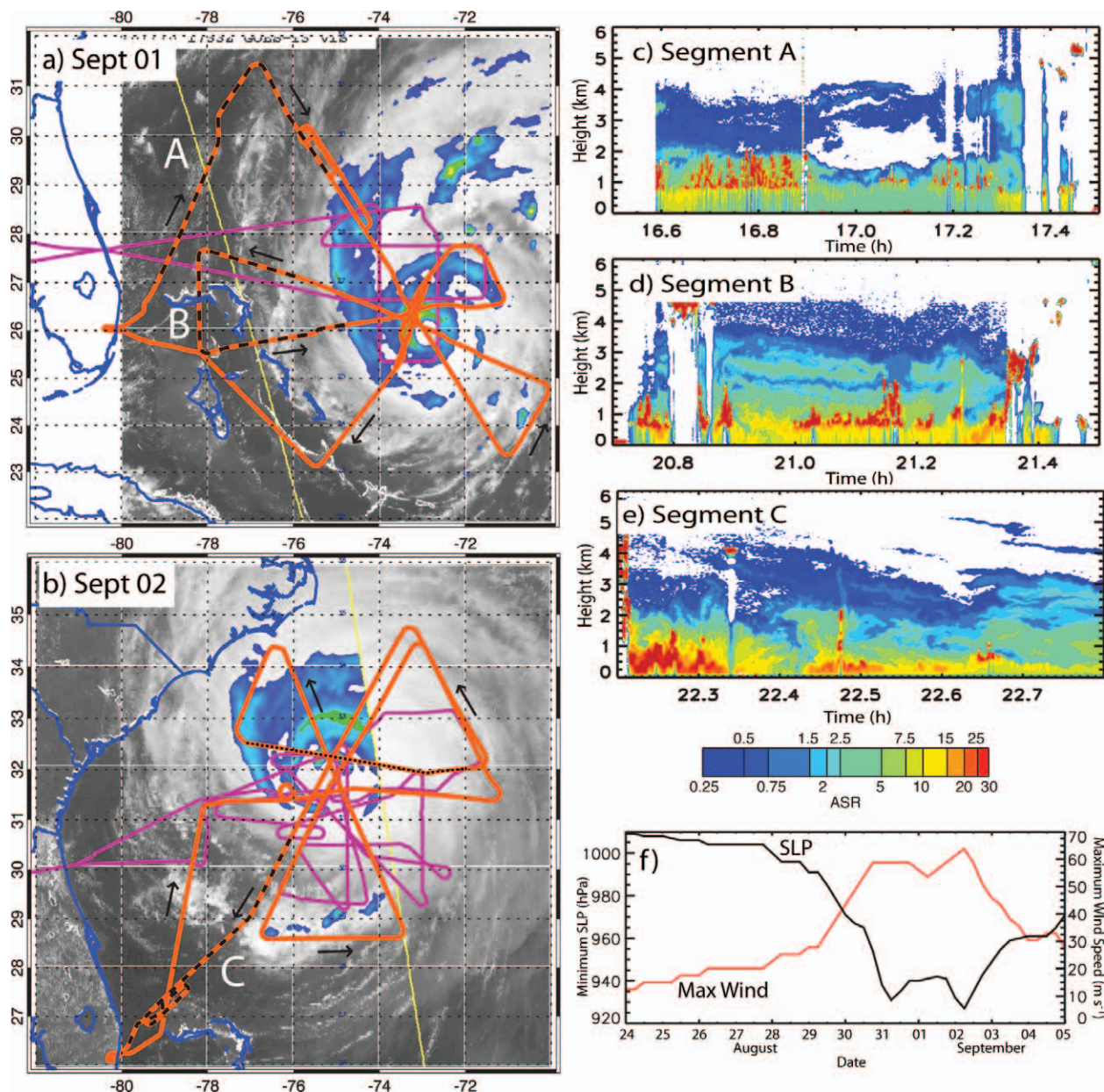


FIG. 10. Flight tracks for (a) the DC-8 and WB-57 on 1 Sep and (b) the DC-8 and GH on 2 Sep. Flight-track segments with a dashed black line show the locations of (c)–(e) corresponding LASE aerosol scattering ratio vertical cross sections. The thin black dotted line along a west–east transect in (b) indicates the location of the radar and microphysical data in Fig. 11. The LASE data show dust extending to up to 4 km on the western side of the storm on both days. (f) Time series of best-track minimum sea level pressure and maximum wind speed (from www.nhc.noaa.gov/2010atlan.shtml). Satellite images are from the NRL TC web page.

rainband, regions with high concentrations in the 4–20- μm -diameter range were observed, suggesting that dust may have been impacting those regions as well.

An interesting question for future research is whether the dust may have played some role in the secondary eyewall formation (SEF) and eyewall replacement cycle on 31 August. While most hypotheses for SEF focus on thermodynamic or dynamical mechanisms (e.g., Montgomery and Kallenbach 1997; Nong and Emanuel 2003; Kuo et al. 2004; Judt and Chen 2010; Huang et al. 2012), Khain et al. (2008, 2010) and Zhang et al. (2009) suggest that aerosols may lead to invigoration of convection on the storm periphery in a way that weakens convection in the eyewall and lowers the intensity of the storm. Hurricane Earl will be an excellent case for evaluating the role of aerosols in SEF.

Genesis of Hurricanes Karl and Matthew. While the genesis of storms was a major science target of GRIP and data were collected for two well-observed events, Karl and Matthew, we provide only a brief summary of these cases here. Additional information on these storms can be found in Davis and Ahijevych (2012), Smith and Montgomery (2012), and Montgomery et al. (2012).

The predepression disturbance that became Hurricane Karl first formed north of South America ($\sim 11^\circ\text{N}$, 60°W) late on 9 September. Coordinated flights between the NSF Gulfstream V (G-V), the NASA GH, and the DC-8 took place on 12 September, with subsequent flights of the G-V and DC-8 on 13–14 September. During this time, the system slowly developed as daily episodes of deep convection formed and then dissipated (Davis and Ahijevych 2012).

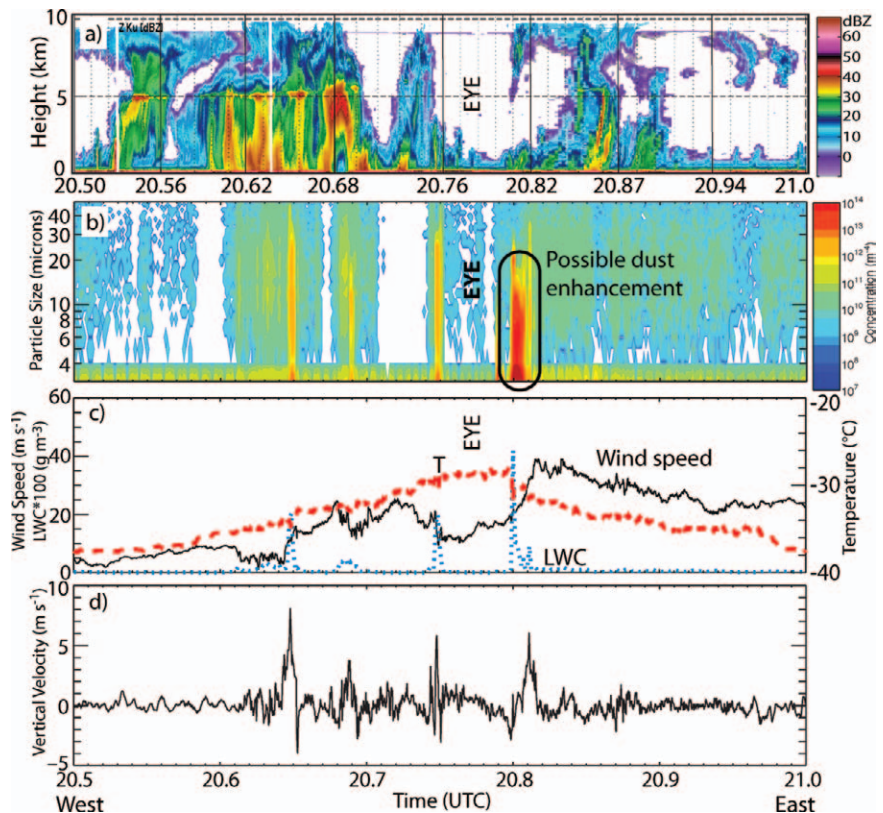


FIG. 11. As in Fig. 9, but for a west-to-east transect across Earl on 2 Sep. Note that, unlike in Fig. 9, the time line for the APR-2 radar is close to, but does not exactly match, that of the in situ data. Impact of aerosols is evident in the very high concentrations of small drops in the eastern eyewall. Flight level for in situ data in (b)–(d) was ~ 10.6 km.

Dropsonde wind analyses at 925 hPa show the vortex evolution from 12 to 14 September overlaid on TRMM Multisatellite Precipitation Analysis (Huffman et al. 2007) rain accumulations for 12–15 September (Fig. 12a). While only 8 flights among the agencies are shown, a total of 16 missions with dropsonde-equipped aircraft were flown into developing Karl between 10 and 14 September.⁵ The dropsonde winds depict the gradual transition from open wave on 12 September to closed tropical storm circulation on 14 September. Episodic convection contributed to the gradual spin up of the circulation through the time of Karl's designation as a tropical storm by the NHC on 14 September, at which point sustained heavy precipitation began near the center of the storm. The storm made landfall near Chetumal, Mexico, on the Yucatan Peninsula midday on 15 September with maximum sustained winds near 28 m s^{-1} .

While Karl was beginning its intensification in the Gulf of Mexico on 16 September, a new disturbance

⁵ The missions consisted of 3 GRIP DC-8 flights, 6 PREDICT G-V flights, 6 NOAA flights (3 for the P-3s, 3 for the G-IV), and 1 U.S. Air Force flight.

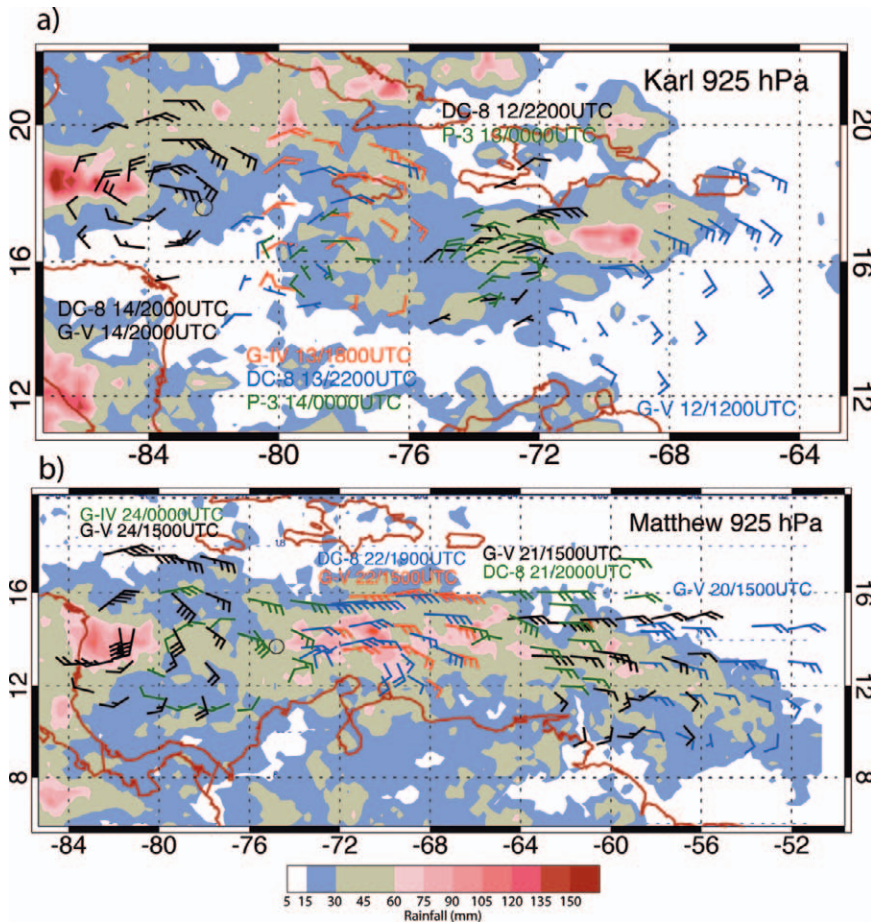


FIG. 12. A summary of dropsonde observations from combined research flights into pregenesis and developed (a) Karl and (b) Matthew at 925 hPa. Dropsonde locations are at the launch latitude/longitude and are time–space corrected to the same time (labeled) using the system zonal phase speed. Colors differentiate aircraft, with the exception of the G-V and DC-8 on 2000 UTC 14 Sep in (a). Open circles indicate the NHC best-track locations of the first tropical depression classification for each storm. Some dropsondes far from the disturbance center have been removed for clarity. Also shown is the TRMM 3B42 accumulated precipitation between 12 and 15 Sep in (a) and 20 and 24 Sep in (b).

was identified in the PREDICT pouch products (Wang et al. 2009) near 10°N, 40°W. Despite the identification of a pouch, significant convection did not begin for two more days. The early stages of Matthew's development were sampled by multiple flights by the NASA, NSF, and NOAA aircraft beginning on 20 September and continuing until landfall on 24 September. Dropsonde data from the DC-8, G-V, and NOAA G-IV (Fig. 12b) show the evolution of the wind field during this period in relation to rainfall derived from the TRMM multisatellite product. Similar to Karl, the dropsonde data show the gradual transformation of strong easterlies associated with the initial wave to the formation of a strong cyclonic circulation prior to landfall. Diurnal cycles of convection occurred from 18 to

23 September followed by a period of sustained convection (Davis and Ahijevych 2012) that produced heavy rainfall associated with Matthew prior to landfall. Tropical Storm Matthew was identified by the NHC by 1800 UTC 23 September.

On 24 September, the GH spent about 8 h over Tropical Storm Matthew (from ~0100 to 0900 UTC), continuously repeating a rotating Fig. 4 pattern with variable leg lengths (Fig. 13a). Northeasterly deep-layer vertical wind shear of $\sim 6 \text{ m s}^{-1}$ produced a marked asymmetry of the precipitation field with intense convection downshear. Examples of HIWRAP data at Ku band (Figs. 13b–e) during this flight show the structure of intense convective bursts that characterized Matthew up to its time of landfall. The most intense burst occurred in pass 5 from 0426 to 0452 UTC in which high reflectivities extended up to near 15 km, causing significant attenuation (reduction of signal) of the reflectivity at lower levels. Pass 9 clearly shows

the convection along the eastern side of the convective system, to the southwest of the estimated center position, with a broad stratiform region at larger radius. The HIWRAP dataset, although still very preliminary, offers great potential for diagnosing storm structure and evolution, particularly when combined with surface wind measurements derived from scatterometry techniques (still to be completed) from HIWRAP in nonprecipitating regions closer to the storm center.

PROMISING AREAS FOR FUTURE RESEARCH. The combined data from GRIP, PREDICT, and IFEX have produced one of the most comprehensive datasets ever obtained on the genesis and rapid intensification of hurricanes in the northern

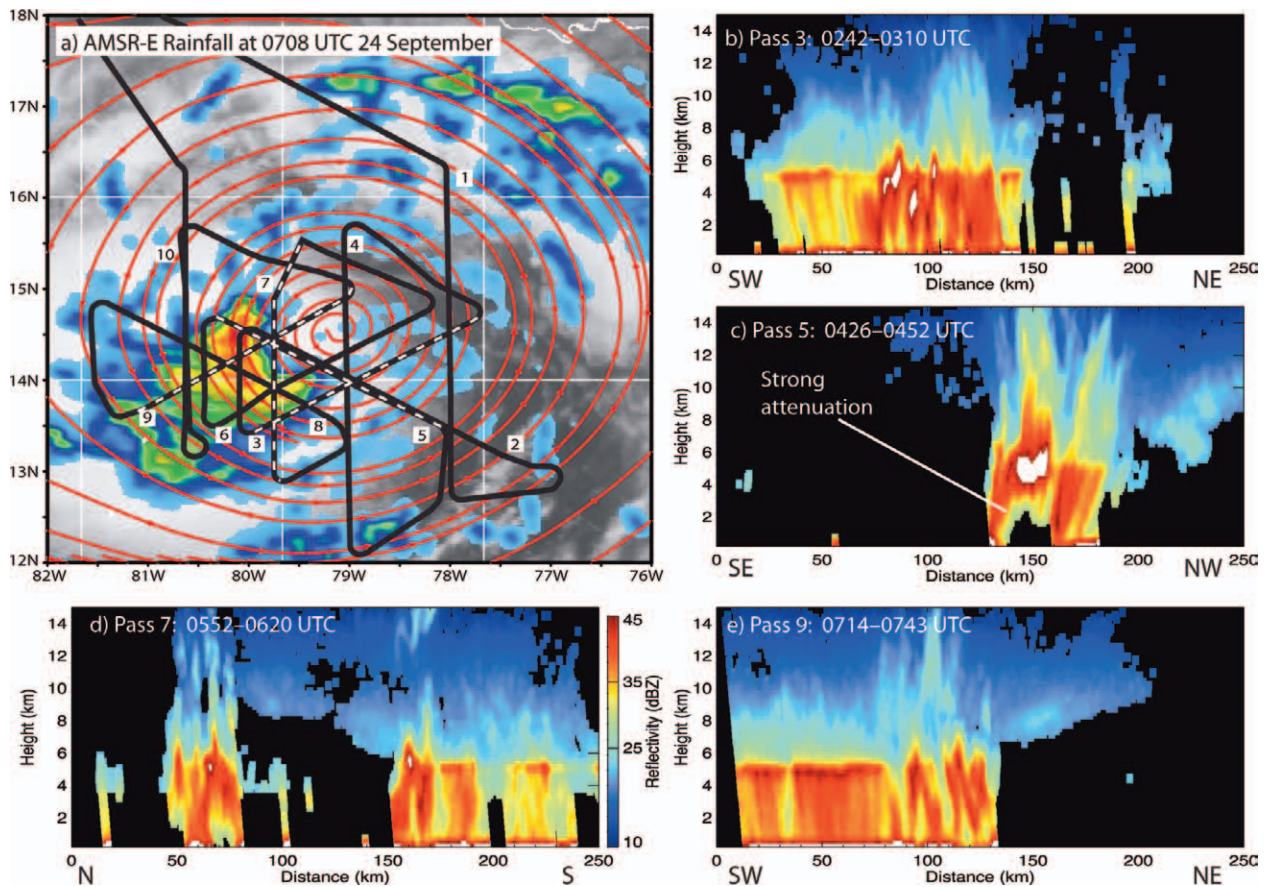


FIG. 13. (a) GOES-13 infrared image for 0715 UTC and AMSR-E rainfall (mm h^{-1}) for 0708 UTC 24 Sep from the NRL TC web page. Superimposed are NCEP GFS–derived storm-relative streamlines at 700 hPa (red lines) and the GH flight track (black lines). The satellite image was shifted $\sim 0.3^\circ$ to the east to account for the 8.5 m s^{-1} westerly storm motion and the 68-min time difference between the GFS analysis and AMSR-E image. (b)–(e) Vertical cross sections of HIWRAP radar reflectivity for the flight legs (3, 5, 7, and 9) corresponding to the indicated times on 24 Sep. Color scale for reflectivity is on the right side of (d). Locations of the flight segments corresponding to these cross sections are shown in (a) by the dashed white lines. Flight segment identification numbers are indicated at the start of the segments.

Atlantic Ocean basin. Extensive airborne sampling of Hurricanes Earl and Karl during their RI phases provided unprecedented information on the evolution of precipitation, kinematic, and thermodynamic fields during a poorly understood stage of development. Multiple flights into Karl and Matthew beginning several days prior to their genesis will allow a comprehensive examination of environmental and inner-core processes leading to storm formation. Data from the suite of remote and in situ sensors, along with satellite data, provide an excellent opportunity to evaluate these physical processes and their representation in numerical forecast models through evaluation of model physics and assimilation of data into models. The observations and simulations will be critical to answering key questions about the relative roles of large-scale environmental factors such as African

easterly waves and their associated wave “pouches,” the SAL, and vertical wind shear versus inner-core processes such as mesoscale stratiform precipitation regions, convective bursts, and vortical hot towers.

GRIP also provided the first demonstration of the value of the GH unmanned airborne system for hurricane research. With its high flight altitude and long flight duration, the GH can serve as a virtual satellite for hurricane observation and monitoring. NASA will follow up on its GRIP GH flights with another investigation called the Hurricane and Severe Storm Sentinel (HS3), which will use two GHs deployed from NASA’s Wallops Flight Facility in Virginia in 2012–14. By deploying from the U.S. East Coast, the GHs will have more direct access to the Atlantic Ocean basin, with on-station times of 15–20 h over western Atlantic storms and 5–10 h over storms in

the central to eastern Atlantic. HS3 will use the GRIP instruments HIWRAP, HAMSR, and HIRAD on one GH for over-storm sampling and will use a cloud physics lidar, interferometer sounder, wind lidar, and dropsonde system on the other GH for environmental sampling. GRIP and HS3 epitomize NASA's unique and complimentary role in continually advancing Earth system science from air and space, create new remote sensing capabilities, and enhance the operational capabilities of other agencies, collaborating with them to advance national Earth science goals.

ACKNOWLEDGMENTS. The GRIP campaign owes its success to the hard work of many individuals who served as mission scientists during the campaign, including John Molinari, Elizabeth Ritchie, Robert Houze Jr., Greg McFarquhar, Richard Blakeslee, and Michael Black. We also would like to thank Bruce Anderson, Aaron Bansemer, Richard Blakeslee, Michael Goodman, Johnny Hall, Svetla Hristova-Veleva, Doug Mach, Robert Rogers, Lin Tian, and Luke Ziemba for their assistance with an earlier draft of the manuscript, and Paul Newman at Goddard for his help in drafting Fig. 1. A portion of this research (Brown, Durden, Lambrihtsen, and Tanelli) was carried out at the Jet Propulsion Laboratory, California Institute of Technology, under a contract with the National Aeronautics and Space Administration.

REFERENCES

- Amarin, R. A., W. L. Jones, S. F. El-Nimri, J. W. Johnson, C. S. Ruf, T. L. Miller, and E. Uhlhorn, 2012: Hurricane wind speed measurements in rainy conditions using the airborne Hurricane Imaging Radiometer (HIRAD). *IEEE Trans. Geosci. Remote Sensing*, **50**, 180–192, doi:10.1109/TGRS.2011.2161637.2012.
- Braun, S. A., 2010a: Comment on “Atlantic tropical cyclogenetic processes during SOP-3 NAMMA in the GEOS-5 global data assimilation and forecast system.” *J. Atmos. Sci.*, **67**, 2402–2410.
- , 2010b: Reevaluating the role of the Saharan air layer in Atlantic tropical cyclogenesis and evolution. *Mon. Wea. Rev.*, **138**, 2007–2037.
- , and L. Wu, 2007: A numerical study of Hurricane Erin (2001). Part II: Shear and the organization of eyewall vertical motion. *Mon. Wea. Rev.*, **135**, 1179–1194.
- , M. T. Montgomery, and Z. Pu, 2006: High-resolution simulation of Hurricane Bonnie (1998). Part I: The organization of vertical motion. *J. Atmos. Sci.*, **63**, 19–42.
- Browell, E. V., and Coauthors, 1997: LASE Validation Experiment. *Advances in Atmospheric Remote Sensing with Lidar: Selected Papers of the 18th International Laser Radar Conference (ILRC), Berlin, 22–26 July 1996*, A. Ansman et al., Eds., Springer, 289–295.
- Brown, S. T., B. Lambrihtsen, A. Tanner, J. Oswald, D. Dawson, and R. Denning, 2007: Observations of tropical cyclones with a 60, 118 and 183 GHz microwave sounder. *Proc. IEEE Int. Geoscience and Remote Sensing Symp. 2007 (IGARSS 2007)*, Barcelona, Spain, IEEE, 3317–3320.
- , —, R. F. Denning, T. Gaier, P. Kangaslahti, B. H. Lim, J. M. Tanabe, and A. B. Tanner, 2011: The High-Altitude MMIC Sounding Radiometer for the Global Hawk Unmanned Aerial Vehicle: Instrument description and performance. *IEEE Trans. Geosci. Remote Sens.*, **49**, 3291–3301, doi:10.1109/TGRS.2011.2125973.
- Chan, K. R., J. Dean-Day, S. W. Bowen, and T. P. Bui, 1998: Turbulence measurements by the DC-8 meteorological measurement system. *Geophys. Res. Lett.*, **25**, 1355–1358.
- Corbosiero, K. L., and J. Molinari, 2002: The effects of vertical wind shear on the distribution of convection in tropical cyclones. *Mon. Wea. Rev.*, **130**, 2110–2123.
- Davis, C. A., and D. A. Ahijevych, 2012: Mesoscale structural evolution of three tropical weather systems observed during PREDICT. *J. Atmos. Sci.*, **69**, 1284–1305.
- Dunion, J. P., and C. S. Velden, 2004: The impact of the Saharan air layer on Atlantic tropical cyclone activity. *Bull. Amer. Meteor. Soc.*, **85**, 353–365.
- Dunkerton, T. J., M. T. Montgomery, and Z. Wang, 2009: Tropical cyclogenesis in a tropical wave critical layer: Easterly waves. *Atmos. Chem. Phys.*, **9**, 5587–5646.
- Evans, C., and Coauthors, 2012: The Pre-Depression Investigation of Cloud-Systems in the Tropics (PREDICT) field campaign: Perspectives of early career scientists. *Bull. Amer. Meteor. Soc.*, **93**, 173–187.
- Frank, W. M., and E. A. Ritchie, 1999: Effects of environmental flow upon tropical cyclone structure. *Mon. Wea. Rev.*, **127**, 2044–2061.
- , and —, 2001: Effects of vertical wind shear on the intensity and structure of numerically simulated hurricanes. *Mon. Wea. Rev.*, **129**, 2249–2269.
- Gunn, R., and B. B. Phillips, 1957: An experimental investigation of the effect of air pollution on the initiation of rain. *J. Meteor.*, **14**, 272–280.
- Halverson, J., and Coauthors, 2007: NASA's Tropical Cloud Systems and Processes experiment: Investigating tropical cyclogenesis and hurricane intensity change. *Bull. Amer. Meteor. Soc.*, **88**, 867–882.
- Huang, Y.-H., M. T. Montgomery, and C.-C. Wu, 2012: Concentric eyewall formation in Typhoon Sinlaku

- (2008). Part II: Axisymmetric dynamical processes. *J. Atmos. Sci.*, **69**, 662–674.
- Huffman, G. J., and Coauthors, 2007: The TRMM Multisatellite Precipitation Analysis (TMPA): Quasi-global, multiyear, combined-sensor precipitation estimates at fine scales. *J. Hydrometeor.*, **8**, 38–55.
- Judt, F., and S. S. Chen, 2010: Convectively generated potential vorticity in rainbands and formation of the secondary eyewall in Hurricane Rita (2005). *J. Atmos. Sci.*, **67**, 3581–3599.
- Kakar, R., M. Goodman, R. Hood, and A. Guillory, 2006: Overview of the Convection and Moisture Experiment (CAMEX). *J. Atmos. Sci.*, **63**, 5–18.
- Kaplan, J., and M. DeMaria, 2003: Large-scale characteristics of rapidly intensifying tropical cyclones in the North Atlantic basin. *Wea. Forecasting*, **18**, 1093–1108.
- Karyampudi, V. M., and T. N. Carlson, 1988: Analysis and numerical simulations of the Saharan air layer and its effect on easterly wave disturbances. *J. Atmos. Sci.*, **45**, 3102–3136.
- , and H. F. Pierce, 2002: Synoptic-scale influence of the Saharan air layer on tropical cyclogenesis over the eastern Atlantic. *Mon. Wea. Rev.*, **130**, 3100–3128.
- Khain, A., N. Cohen, B. Lynn, and A. Pokrovsky, 2008: Possible aerosol effects on lightning activity and structure of hurricanes. *J. Atmos. Sci.*, **65**, 3652–3677.
- , B. Lynn, and J. Dudhia, 2010: Aerosol effects on intensity of landfalling hurricanes as seen from simulations with the WRF model with spectral bin microphysics. *J. Atmos. Sci.*, **67**, 365–384.
- Koch, G. J., and Coauthors, 2010: Field testing of a high-energy 2-mm Doppler lidar. *J. Appl. Remote Sens.*, **4**, 043512, doi:10.1117/1.3368726.
- Kuo, H.-C., L.-Y. Lin, C.-P. Chang, and R. T. Williams, 2004: The formation of concentric vorticity structures in typhoons. *J. Atmos. Sci.*, **61**, 2722–2734.
- Lance, S., C. A. Brock, D. Rogers, and J. A. Gordon, 2010: Water droplet calibration of the cloud droplet probe (CDP) and in-flight performance in liquid, ice and mixed-phase clouds during ARCPAC. *Atmos. Meas. Tech.*, **3**, 1683–1706.
- Li, L., G. Heymsfield, J. Carswell, D. Schaubert, M. Mclinden, M. Vega, and M. Perrine, 2011: Development of the NASA High-Altitude Imaging Wind and Rain Airborne Profiler. *Proc. 2011 IEEE Aerospace Conf.*, Big Sky, MT, Aerospace and Electronic Systems Society, 8 pp., doi:10.1109/AERO.2011.5747415.
- Montgomery, M. T., and R. J. Kallenbach, 1997: A theory for vortex Rossby waves and its application to spiral bands and intensity changes in hurricanes. *Quart. J. Roy. Meteor. Soc.*, **123**, 435–465.
- , and Coauthors, 2012: The Pre-Depression Investigation of Cloud-Systems in the Tropics (PREDICT) Experiment: Scientific basis, new analysis tools, and some first results. *Bull. Amer. Meteor. Soc.*, **93**, 153–172.
- Nong, S., and K. A. Emanuel, 2003: A numerical study of the genesis of concentric eyewalls in hurricane. *Quart. J. Roy. Meteor. Soc.*, **129**, 3323–3338.
- Reasor, P. D., and M. D. Eastin, 2012: Rapidly intensifying Hurricane Guillermo (1997). Part II: Resilience in shear. *Mon. Wea. Rev.*, **140**, 425–444.
- , M. T. Montgomery, F. D. Marks Jr., and J. F. Gamache, 2000: Low-wavenumber structure and evolution of the hurricane inner core observed by airborne dual-Doppler radar. *Mon. Wea. Rev.*, **128**, 1653–1680.
- , —, and L. D. Grasso, 2004: A new look at the problem of tropical cyclones in vertical shear flow: Vortex resiliency. *J. Atmos. Sci.*, **61**, 3–22.
- Rogers, R., and Coauthors, 2006: The Intensity Forecasting Experiment: A NOAA multiyear field program for improving tropical cyclone intensity forecasts. *Bull. Amer. Meteor. Soc.*, **87**, 1523–1537.
- , and Coauthors, 2013: NOAA's Hurricane Intensity Forecasting Experiment: A progress report. *Bull. Amer. Meteor. Soc.*, in press.
- Rosenfeld, D., 1999: TRMM observed first direct evidence of smoke from forest fires inhibiting rainfall. *Geophys. Res. Lett.*, **26**, 3105–3108.
- Sadowy, G. A., A. C. Berkun, W. Chun, E. Im, and S. L. Durden, 2003: Development of an advanced airborne precipitation radar. *Microwave J.*, **46**, 84–98.
- Smith, R. K., and M. T. Montgomery, 2012: Observations of the convective environment in developing and non-developing tropical disturbances. *Quart. J. Roy. Meteor. Soc.*, **138**, 1721–1739.
- Uhlhorn, E. W., and P. G. Black, 2003: Verification of remotely sensed sea surface winds in hurricanes. *J. Atmos. Oceanic Technol.*, **20**, 99–116.
- Wang, Z., M. T. Montgomery, and T. J. Dunkerton, 2009: A dynamically-based method for forecasting tropical cyclogenesis location in the Atlantic sector using global model products. *Geophys. Res. Lett.*, **36**, L03801, doi:10.1029/2008GL035586.
- Zhang, H., G. M. McFarquhar, W. R. Cotton, and Y. Deng, 2009: Direct and indirect impacts of Saharan dust acting as cloud condensation nuclei on tropical cyclone eyewall development. *Geophys. Res. Lett.*, **36**, L06802, doi:10.1029/2009GL037276.
- Zipser, E. J., and Coauthors, 2009: The Saharan air layer and the fate of African easterly waves—NASA's AMMA field study of tropical cyclogenesis. *Bull. Amer. Meteor. Soc.*, **90**, 1137–1156.